Phosphorus Liver MRSI at 3 T Using a Novel Dual-Tuned Eight-Channel ^{31}P/^{1}H Coil

Anshuman Panda,[1,2] Scott Jones,[1,2] Helmut Stark,[3] Rahul S. Raghavan,[1] Kumar Sandrasegaran,[2] Navin Bansal,[1,2] and Ulrike Dydak[1,2]*

Although phosphorus-31 (^{31}P) magnetic resonance spectroscopy holds potential as noninvasive tool to monitor treatment response of liver malignancies, the lack of appropriate coils has so far restricted its use to liver lesions close to the surface. A novel eight-channel phased-array dual-tuned ^{31}P/^{1}H coil that can assess ^{31}P metabolism in deeper liver tissue as well is presented in this article. Analysis of its performance demonstrates that this coil can provide good sensitivity across a width of 20 cm, thereby enabling magnetic resonance spectroscopic imaging (MRSI) scans that can fully cover axial views of the abdomen in lean subjects. In vivo results and reproducibility of ^{31}P MRSI at 3 T of axial slices covering the full depth of the liver are shown in healthy volunteers. To minimize intrasubject and intersubject data variability, spectra are corrected for coil sensitivities. Methods to maximize the reproducibility of coil placement and spectroscopic planning are discussed. The phosphomonoesters/phosphodiesters ratio calculated in healthy volunteers has an average intrasubject variation of 23% averaged over voxels selected from the entire liver. Finally, the feasibility of using the coil in the clinic is shown by preliminary ^{31}P liver MRSI data obtained from a patient with hepatocellular carcinoma. Magn Reson Med 68:1346–1356, 2012. © 2012 Wiley Periodicals, Inc.

Key words: ^{31}P MRSI; liver cancer; phased-array coil; dual-tuned coil

INTRODUCTION

Inflammatory and neoplastic liver diseases affect liver metabolism, thereby altering the intracellular concentration of phosphorus-31 (^{31}P) metabolites (1). Therefore, information on regional changes in ^{31}P metabolites in the liver, as obtained by magnetic resonance spectroscopy (MRS), can help in diagnosis and follow-up of various liver diseases (2). As the ratio of phosphomonoesters (PME) to phosphodiesters (PDE) differs significantly between malignant and healthy liver tissue (3), ^{31}P MRS may be a valuable noninvasive monitoring tool to assess

[1]School of Health Sciences, Purdue University, West Lafayette, Indiana, USA.
[2]Departmemt of Radiology and Imaging Sciences, Indiana University School of Medicine, Indianapolis, Indiana, USA.
[3]Stark Contrast, MRI Coils Research, Erlangen, Germany.

*Correspondence to: Ulrike Dydak, PhD, School of Health Sciences, Purdue University, 550 Stadium Mall Drive, West Lafayette, IN 47907, USA. E-mail: udydak@purdue.edu

early treatment response in targeted radiation therapy (e.g., selective internal radiation therapy with Yttrium-90 (4) and stereotactic body radiation therapy (5)), for which standard image-based monitoring techniques are not conclusive for up to 6 months (6,7).

For the most part, three types of coils have been used for in vivo ^{31}P spectroscopy. The simplest are ^{31}P single-channel surface coils (8–14), which in the past were often single-tuned ^{31}P coils, but today are mostly dual tuned to allow for ^{1}H imaging for localization. The second type are ^{31}P birdcage coils (15–17), which are mainly used for ^{31}P brain spectroscopy. Finally, the third type are ^{31}P phased-array coils (18), which currently are primarily designed and used for human cardiac spectroscopy. In 1989, an early article by Nakada et al. (19) demonstrated abdominal ^{31}P MRS using a zigzag coil design for stomach ^{31}P NMR. Later studies used a "dual-tuned ^{1}H/^{31}P Heart/Liver Coil" on a 1.5 T system (20); however, the manufacturer of the coil has since discontinued its production. That coil consisted of a single plate with one ^{31}P transmit element and a quadrature ^{31}P receive element consisting of a loop and butterfly combination, resulting in a single channel of quadrature output. To date, however, most of the published ^{31}P spectroscopy data of liver and abdomen have been acquired using single channel surface coils.

Single-channel surface coils, when small enough to benefit from good signal-to-noise ratio (SNR), suffer from limited sensitivity in deeper tissue (21). Furthermore, if MRS scans need to be performed in multiple locations, the coil has to be moved for each scan. Moving the coil to acquire multiple datasets increases the scan time and introduces reproducibility errors. When the ^{1}H-tuned part of a dual-tuned coil is a surface coil as well, anatomic image coverage is restricted. As such, to acquire proton images of the entire abdomen in a ^{31}P MRS exam, one is restricted to using the body coil of the scanner, which usually has poor SNR. Furthermore, to minimize motion due to breathing, patients are often expected to lie in prone position, which is not very comfortable for long scans. Therefore, a coil is needed that can overcome the limitations of existing surface coils: one that provides coverage for ^{31}P liver spectroscopy and ^{1}H imaging across the entire abdomen, reduces the coil-setup error, and minimizes patient discomfort during long scans.

To address these limitations, we have designed an eight-channel phased-array dual-tuned ^{31}P/^{1}H coil that wraps around the torso and covers the whole liver, thus eliminating the need for repositioning coils within a liver examination. A phased-array design was chosen incorporating eight ^{31}P channels and two ^{1}H channels
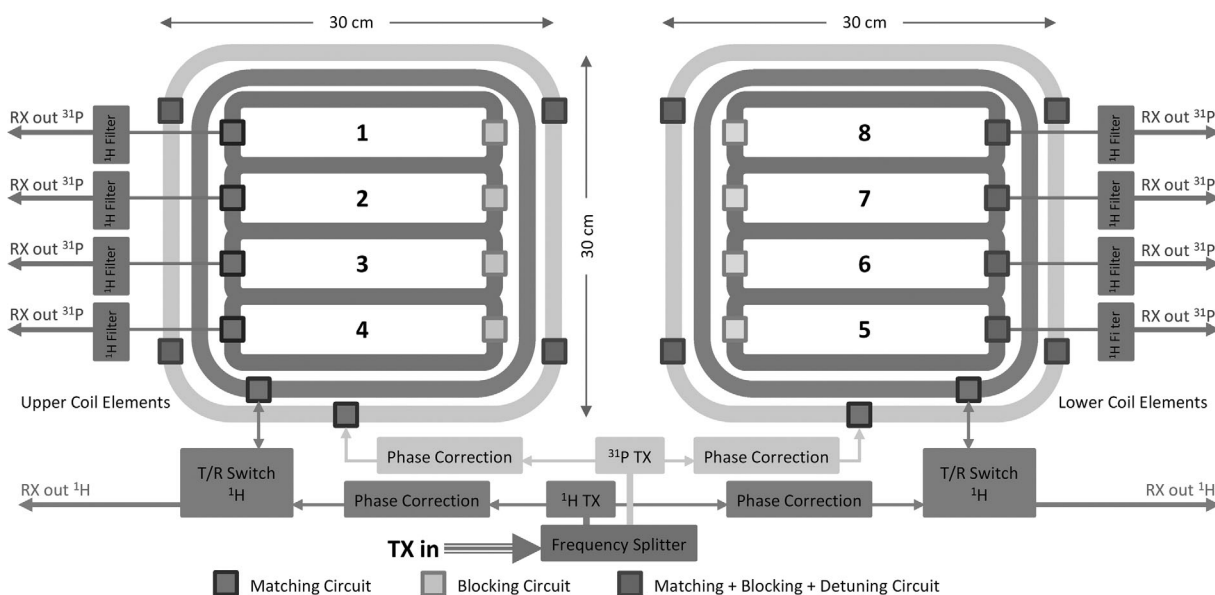
FIG. 1. Schematic diagram of the eight-channel dual-tuned ^{31}P/^{1}H coil. The coil consists of two plates, shown in the diagram as upper coil and lower coil elements, respectively. Each plate consists of one ^{1}H TX-RX element, one ^{31}P TX, and four ^{31}P RX coil elements. The numbers 1–8 correspond to the individual ^{31}P RX channels.

for proton imaging as well as decoupling to provide a higher SNR and larger coverage (18,22). This article presents results on quality and coverage of in vivo ^{31}P liver MRSI data obtained with this novel coil at 3 T. Specifically, we examine factors and technical constraints that affect data quality and reproducibility, including separation between the anterior and posterior coils and reproducibility of placing the spectroscopic imaging grid. We present 2D ^{31}P MRSI data from axial slices covering the full cross section of the liver in both healthy volunteers and patients, acquired with an optimized approach with regard to coil setup, acquisition parameters, and processing of the data.

Finally, we show data acquired in a patient with hepatocellular cancer (HCC) to demonstrate the sensitivity of our 2D ^{31}P MRSI protocol and coil to metabolic changes in malignant liver tissue.

METHODS

Hardware

A dual-tuned eight-channel ^{31}P/^{1}H coil (built by Stark Contrast MRI Coils Research, Erlangen, Germany, according to our design specifications) was used for both ^{31}P MRSI and ^{1}H imaging on a Siemens 3 T TIM Trio whole body scanner (Siemens Healthcare, Erlangen, Germany). The coil array consists of two plates (30 × 30 cm^{2}), each with four ^{31}P receive (RX) elements ($\sim$ 24 × 20 cm^{2}) with filters for proton decoupling, one ^{31}P transmit (TX) element ($\sim$ 30 × 30 cm^{2}), and one ^{1}H TX-RX element ($\sim$ 27 × 25 cm^{2}) (Fig. 1). The ^{1}H and the ^{31}P transmit coils on the anterior and posterior plates form Helmholtz pairs. They all share one TX-connector, thus distributing the power to the two coils using this single connector. The transmit signal passes through a frequency filter and splitter to the respective ^{1}H and ^{31}P transmit circuits. The four independent ^{31}P RX channels per plate are

attached to patient table connectors by means of a common output cable. The eight ^{31}P and two ^{1}H channels are decoupled using preamplifier decoupling. Neighboring coils are decoupled by a common rod and an adjusted capacitor to better than −12 to −20 dB. This coupling is load dependent due to common noise resistance and thus noise correlation for common areas. Additional decoupling is achieved by preamplifier decoupling used between all RX elements. In total, decoupling between all elements is better than −15 dB, which is sufficient for adequate SNR and the use of parallel imaging techniques. The coils are matched to load. With a common load for all elements, matching (S-parameters: S_{11}, S_{22} ... S_{88}) results in < -14 dB (or <0.2 on a linear scale).

The signal is phase corrected and sent to the coils through respective matching circuits. Each coil consists of matching, blocking, and detuning circuits to ensure the appropriate coils are active and tuned for the specific acquisition. The ^{1}H coil elements are further capable of proton decoupling, by transmitting at high power at the ^{1}H frequency during reception of ^{31}P signal. This is achieved by decoupling of ^{1}H TX and ^{31}P RX coils and blocking circuits for ^{1}H RX frequency, adding very high attenuation filters to reduce ^{1}H signal on the ^{31}P receive path to avoid saturating the ^{31}P preamplifiers, and placing filters and ^{31}P preamplifiers in shielded boxes to minimize B_1 coupling to the ^{1}H decoupling field. Applying ^{1}H power between acquisition windows to provide nuclear Overhauser enhancement of ^{31}P spins is also possible. Finally, plugging in this coil disables the scanner's body coil so that only the ^{1}H channel of the dual-tuned coil can be used to acquire ^{1}H images.

For scan setup, the two plates of the coil wrap around the torso of the subject with four ^{31}P receive elements on the back and four on the front to increase sensitivity
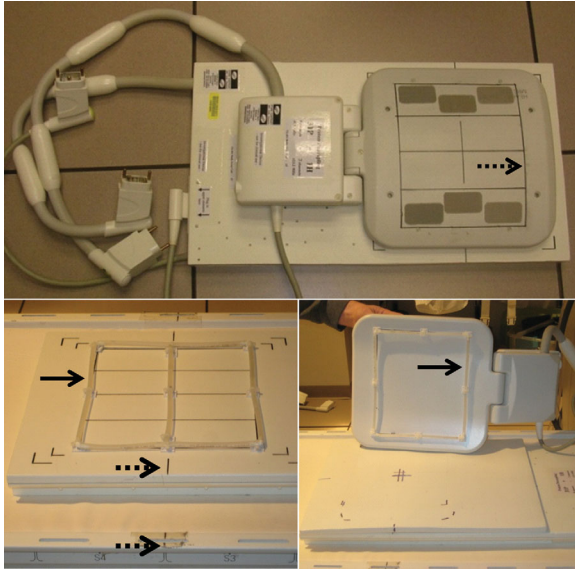
FIG. 2. Photograph of the coil with top and bottom plate and respective connectors. The placement of water-filled fiduciary markers around the coil circumference (solid arrows) and permanent markers on the scanner bed and coil surface (dashed arrows) can also be seen in the picture. [Color figure can be viewed in the online issue, which is available at wileyonlinelibrary.com.]

throughout the abdomen. The top plate is free to move up and down with the subject's abdominal movement during respiration, but this movement is minimized by adding straps to hold the plate in place. Furthermore, subjects are instructed to take short, shallow breaths instead of long, deep breaths during data acquisition. The coil was designed so that hardware performance is not degraded by slight respiratory movement of the top coil although typical breathing artifacts are still seen in images. To increase the reproducibility of coil positioning, water-filled fiduciary markers were placed on both anterior and posterior coil plates around the coil circumference to be used as reference points for acquisition planning and postprocessing alignment (Fig. 2). Permanent markers on the scanner bed and coil surface were used to ensure that the patient is placed reproducibly with respect to the coil at the exact same location each time.

A 10-L plastic carboy filled with 10-mmol/L potassium dihydrogen phosphate (Pi) solution was used as a phantom for initial pulse sequence development and radio frequency (RF) transmitter calibration. NaCl (75 mmol/L) was also added to the phantom solution to match in vivo loading and conductivity properties in accordance with the American College of Radiology (ACR) body phantom recommendation (23). Finally, 0.04 g/L of $NiCl_2$ was added to reduce the T_1 relaxation time of ^{31}P (9).

Volunteers and Patients

Three healthy volunteers (age 30 $\pm$ 10 years, weight 65 $\pm$ 7 kg) were scanned for in vivo data quality and reproducibility analysis using our coil. Each subject was scanned three times, generally in the afternoon, at least

2–3 h after lunch. No specific fasting was required of the subjects. In addition, two patients with HCC were scanned to investigate the efficacy of the coil for clinical applications. The study was approved by the institutional review board, and all subjects gave written informed consent before participating in the study.

^1H Imaging

^1H images for spectroscopy localization and postacquisition analysis were acquired using a gradient recalled echo sequence (pulse repetition time (TR) of 23 ms, echo time (TE) of 3.69 ms, 6.0-mm slice thickness, 15-mm interslice gap, and 10 slices; total imaging time $\sim$ 1 min). The prespectroscopy localization slices were acquired in all three directions using a field of view (FOV) of 450 $\times$ 450 mm^2. The large size of the FOV was chosen to include signal from the fiduciary markers on the coil plates. The MRSI grid was then placed on the images by using these markers as reference points (Fig. 3). A second set of
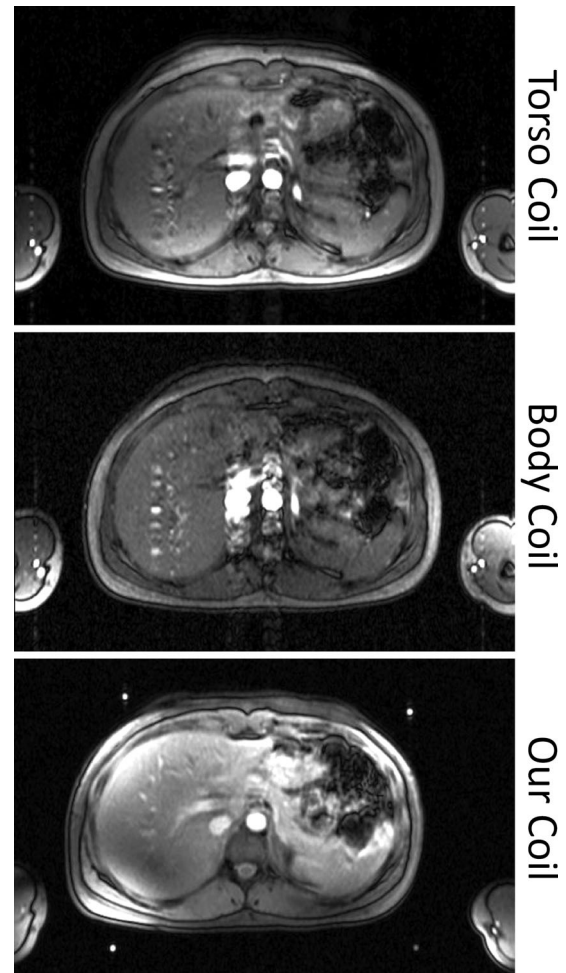

FIG. 3. ^1H images obtained from a dedicated torso coil, the scanner's body coil, and our coil using the same acquisition protocol (gradient echo sequence). The four bright spots on each corner of the image obtained with our coil correspond to the water-filled fiduciary markers placed on the coil to ensure reproducible MRSI planning and acquisition. The new coil provides high-quality ^1H MRI images, adequate for most clinical imaging protocols in the liver.

images was acquired immediately after the long MRSI acquisition using the identical geometric setup and FOV (400 × 400 mm^2) as the MRSI scan to check for any changes in the position of the subject.

Standard MR imaging protocols from our clinical routine were used to validate imaging results with the dual-tuned coil, and image quality was compared to that obtained with standard ^{1}H coils. To assess whether the ^{1}H liver images acquired with our coil are of sufficient quality for clinical needs, a comparison between our coil, the body coil, and the Siemens standard torso coil was performed. SNR values were compared using the following equation:

$$\text{SNR} = \frac{|S_{\text{ROI}} - S_{\text{Bkg}}|}{\sigma_{\text{Bkg}}} \quad [1]$$

Here, S_{ROI} is the signal intensity obtained from a region of interest (ROI) area placed in the liver or muscle tissue of the images, S_{Bkg} is the signal intensity obtained from the background region (outside the coil FOV and free from any artifact noise), and σ_{Bkg} is the standard deviation of the background noise calculated from the S_{Bkg} ROI.

^{31}P 2D MRSI

For all ^{31}P scans (sensitivity calibration, Specific absorption rate [SAR] measurements, and phantom and in vivo data acquisition) a 2D-slice-selective free-induction-decay (FID) sequence was used to collect ^{31}P MRS data with the following parameters: TE = 2.3 ms, TR = 1 s, FOV = 400 × 400 × 30 mm^3, and a nominal voxel size of 25 × 25 × 30 mm^3, yielding an effective voxel size of 45 × 45 × 30 mm^3 when the MRSI spatial response function is considered (24). Manual shimming was performed before each scan, and datasets were collected with free breathing. Each FID was acquired with 2048 complex points and a bandwidth of 5000 Hz. No ^{1}H–^{31}P decoupling was applied in this initial study. The acquisition took about 24 min for 30 weighted averages. The first point of each FID was used to determine the relative phase of each coil and to phase correct the data before combining the signals using a weighted sum-of-squares method (22), which has been shown to yield higher SNR spectra than an unweighted combination. The magnitude of the first point was used as an estimate of the signal amplitude, which was then used to calculate the corresponding weights for the individual coils. This way, the coil with the greatest signal was given the largest weight. The resulting FID summation was then zero filled to 4096 data points. Finally, an exponential filter of 25-Hz line-broadening and zero- and first-order phase correction were applied to the combined signal.

Specific Absorption Rate Calculation

To ensure patient safety, SAR measurements were performed for both the ^{1}H imaging and ^{31}P spectroscopy protocols on a phantom. The SAR levels produced with this coil were determined by using the Food and Drug Administration recognized calorimetric method described in the National Electrical Manufacturing Association standards (25). Both the ^{1}H imaging sequences and ^{31}P spectroscopy sequences were run repeatedly for about an hour each to achieve a measurable increase in temperature. The energy absorbed by the phantom was calculated from the specific absorption coefficient of the water and the temperature increase between the beginning and end of the scan.

Determination of Maximum Sensitive Depth and Sensitivity Correction

To determine the maximum depth at which the ^{31}P coil elements are still sensitive, we stacked two 10-L phantom carboys, both 15 cm in height and both filled with the same concentration (10 mmol/L) of potassium dihydrogen phosphate (inorganic phosphate - Pi) solution. ^{31}P MRSI datasets were collected with the anterior and posterior coil plates separated by 30 cm (Fig. 4a). As the two transmit coils on the anterior and posterior plates share one TX-connector, it was not possible to merely turn one of them off. Therefore, the only way to assess the effect of both the TX and RX elements on each plate independently was to separate the plates as far as possible during data acquisition. A separation of 30 cm between the coils was large enough to ensure that the data only reflected the sensitivity of the anterior or the posterior plate individually and not the combination of the two plates.

The total area under the Pi peak was used to calculate Pi metabolite maps and to determine coil characteristics. In subsequent sections, metabolite maps of the inorganic phosphate peak obtained from this homogeneous phantom will be referred to as sensitivity maps. To a first approximation, the observed signal variation is due to variation in the flip angle with depth from the TX side plus variation of the RX coils' sensitivity. Figure 4a shows the typical gradual drop in signal intensity as a function of distance from the coil. The signal is scaled to the maximum signal recorded. Coil inhomogeneity correction was performed by a technique similar to Ref. 26. Any signal below 25% was considered noise and was removed from the sensitivity maps. Inverse sensitivity maps were created to obtain sensitivity correction matrices for both the anterior and posterior coil plates (each containing four ^{31}P channels). These matrices were then used to correct for variations in coil sensitivity for both the phantom and in vivo ^{31}P data. For SNR determination of phantom spectra, the amplitude of the Pi peak was used as signal, and the standard deviation of the real signal in a 20-ppm-wide baseline region was used as noise.

Data Quantification and Variability Assessment

^{31}P spectroscopic data were quantified using the AMARES routine (advanced method for accurate, robust, and efficient spectral fitting of MRS data with use of prior knowledge) (27) in the fitting software jMRUI (28). The model used in jMRUI to fit the peaks was a Gaussian peak model with soft constraints on phase, line width, and J-coupling frequency similar to the method

Coil Sensitivity Analysis
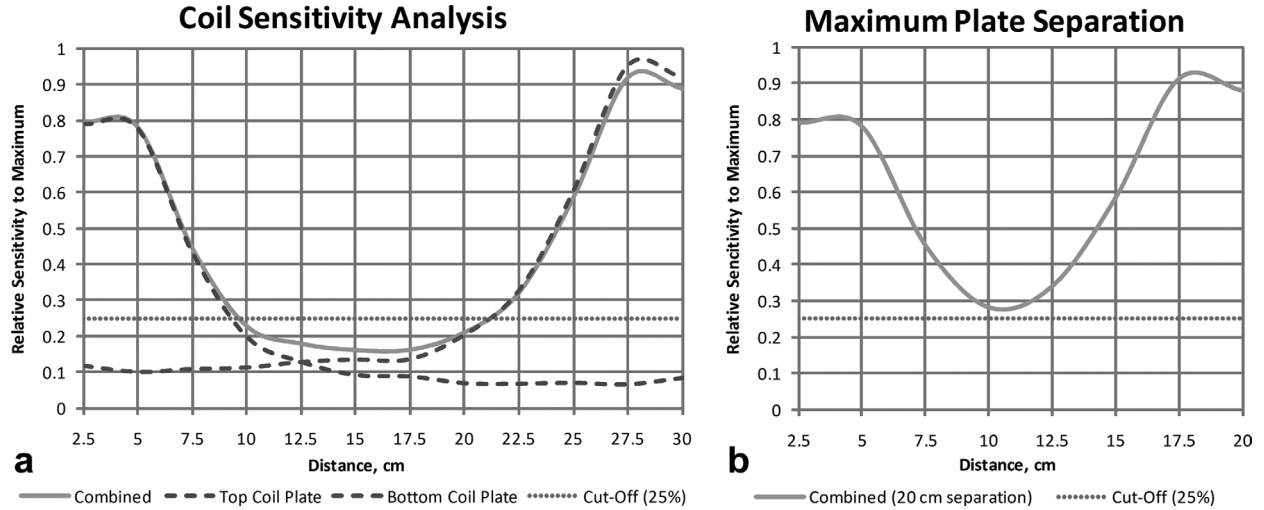

Maximum Plate Separation

FIG. 4. Anterior and posterior coil plate sensitivities. **a**: The measured combined sensitivity of the top and bottom coils (solid line) for a coil plate separation of 30 cm, as a function of distance from the top plate. The dashed lines show the sensitivity profiles of the individual top and bottom plates. **b**: The calculated sensitivity profile derived from sensitivities of individual coil plates for a separation of 20 cm. The dotted line in both plots represents an empirically calculated cut off value of 25% below which no signal could be quantified.

described in Ref. 29. The acquisition delay of 2.3 ms in the current protocol creates a baseline distortion in the acquired ^{31}P spectrum, which was modeled by treating the first 11 points of the FID as baseline before quantification of the peaks in the time domain. For in vivo data, seven metabolites were quantified: β-adenosine triphosphate (β-ATP), α-adenosine triphosphate (α-ATP), γ-adenosine triphosphate (γ-ATP), phosphocreatine (PCr), inorganic phosphate (Pi), PME, and PDE. To examine intrasubject variability, three scans were performed on separate days on the same subject with the same protocol. Ten to 12 voxels (depending on the subject size) from various locations in the liver were chosen for data quality and reproducibility assessment. Figure 5 illustrates the reproducibility of the scan setup for one subject scanned on two different days. Spectra from the highlighted voxels were selected for data analysis. As the PME/PDE ratio is most sensitive to changes in tumor metabolism (3) and is thus our primary marker for tumor response analysis, this ratio was used for variability assessment. Data variability per voxel between two scans on different days for the same subject is given as:

$$V_{A_iB_i} = \frac{|S_{A_i} - S_{B_i}|}{\overline{S}_{A_iB_i}} \qquad [2]$$

Here, $V_{A_iB_i}$ is the variability in the PME/PDE ratio for voxel i (where i corresponds to the voxel at the same anatomic location in both scans A and B), S_{A_i} and S_{B_i} are the PME/PDE ratios for voxel i calculated for scans A and B, respectively, and $\overline{S}_{A_iB_i}$ is the mean of the PME/PDE ratio from voxel i for the two scans. The average variability between two scans was then calculated by averaging the values obtained for the selected voxels:

$$\overline{V}_{AB} = \frac{\sum_{i=1}^{n} V_{A_iB_i}}{n} \qquad [3]$$

Here, $\overline{V}_{AB}$ is the average variability in the PME/PDE ratio for the same subject between scan A and B, and n is the number of selected voxels quantified ($n \approx 10$) for a subject.

RESULTS

Specific Absorption Rate of the Coil

The coil produced SAR levels of less than 1.0 W/kg for both the ^{31}P spectroscopic sequence and the ^1H imaging sequence. The precision of the thermocouple used for measuring temperature was ±0.1°C. This accuracy introduced ~ 10% error in the SAR measurement. The calculated SAR values including the measurement errors were much lower than the smallest SAR limitation of 4 W/kg recommended by the Food and Drug Administration. Therefore, the coil met all the safety requirements for in vivo data collection using the tested sequences.

^1H Imaging

Figure 3 shows the same transverse slice through the liver in the same volunteer acquired with the same ^1H imaging sequence (described above) using three different coils: a torso coil, the body coil, and our phased-array coil. The SNR was calculated over several ROI locations in liver tissue and muscle tissue. While the SNR remains best for the torso coil (SNR of 89 for liver tissue and SNR of 133 for muscle tissue), our coil performs better (SNR of 76 for liver tissue and SNR of 50 for muscle tissue) than using the in-built body coil (SNR of 30 for liver tissue and SNR of 19 for muscle tissue). In practical terms, a radiologist (KS) deemed the image quality of our coil good enough that repositioning of patients for separate ^1H imaging using the standard torso coil was unnecessary for clinical scanning.
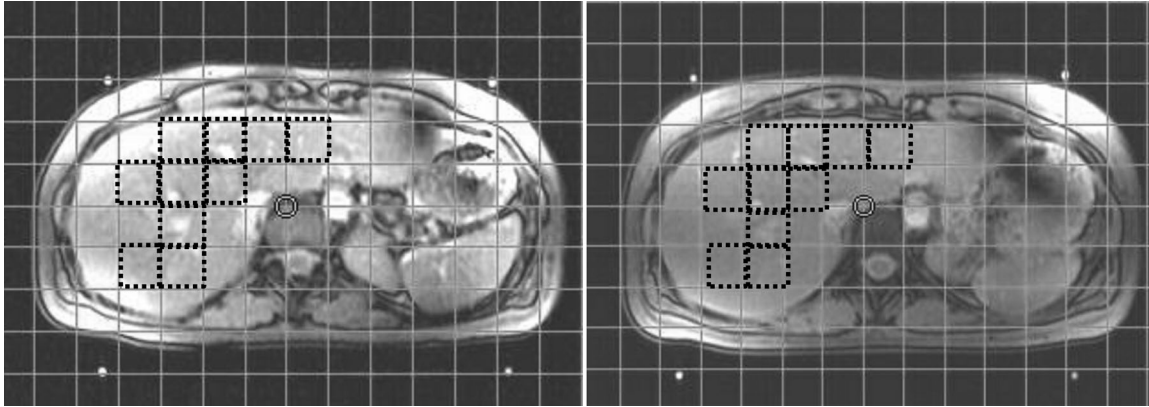
FIG. 5. ^{31}P MRSI scan setups in the same subject on two different days. The voxels chosen for the reproducibility analysis are highlighted with dashed lines. The signals from fiduciary markers used to place the spectroscopy grid can be observed on the four corners of both images.

Sensitivity Correction and Maximum Depth Calculation

To calculate the maximum sensitive depth, any signal below 25% of the maximum was considered noise. This threshold was calculated from the SNR analysis of the stacked phantom experiment described in the methods sections. For an SNR of 30 or less in the phantom experiment, the Pi peak was indistinguishable from the noise. Therefore, SNR of less than 30 was considered the cutoff for sensitivity below which any signal was considered noise. In our phantom experiment, this SNR value corresponded to a value of 25% of the maximum area under the Pi peak. It can be observed from Fig. 4 that the bottom (posterior) coil is slightly more sensitive compared to the top (anterior) coil. It can also be observed in Fig. 4a that at a depth of about 10 cm from the top coil and 8.75 cm from the bottom coil, less than 25% of the maximum signal was recorded. For the maximum depth calculation, the data from anterior and posterior coil plates were combined using the sum-of-squares technique while progressively reducing the separation between the coil plates in the calculation. It can be seen in Fig. 4b that a separation of the plates of 20 cm results in the entire sensitivity profile being above the cut off threshold of 25%. This implies that the maximum separation of the coil plates that maintains sensitivity throughout the whole axial FOV is 20 cm. Figure 6 shows ^{31}P metabolite maps of a phantom before and after sensitivity correction using the correction matrices obtained as described in the Materials and Methods section.

In Vivo ^{31}P MRSI: Healthy Volunteers

Figure 7 shows the placement of various coil elements with respect to the human abdomen superimposed on a localizer image acquired with the ^{1}H channels of our coil. It also shows the ^{31}P spectra of three voxels from deep liver tissue (plus one from abdominal muscle for comparison) and metabolite maps, generated by plotting the area under the peaks of various ^{31}P metabolites over the whole slice. As expected, the metabolite maps illustrate that PCr signal originates mainly from muscle tissue, while Pi, β-ATP, α-ATP, and γ-ATP are concentrated in muscles, liver, and spleen. We do see some PCr signal in the voxels inside the liver, which is due to the point spread function and/or breathing artifacts. The contribution from breathing could likely be minimized with respiratory gating. The PCr distribution, resulting from the point spread function, could potentially be used to estimate and remove contamination of skeletal muscle signal to adjacent liver voxels. In liver voxels where signal from PCr was not higher than the background, the PCr signal was excluded from reproducibility or quality assessment.

Table 1 summarizes the variability results for the PME/PDE ratios obtained for three healthy volunteers. The subjects were scanned three times on different days using the same protocol. The PME/PDE ratio calculated from these healthy volunteers had an average scan-to-scan variation of 21.5–24.6% (with maximum variation of 27.8%) over three scans for 10 different voxel locations within the liver. Table 2 summarizes the average PDE/β-ATP, Pi/β-ATP, and PME/β-ATP ratios for the three scans, and gives the average variation of these ratios between scans for the same three healthy volunteers. Overall, the ratios of PDE/β-ATP, Pi/β-ATP, and PME/β-ATP showed an average variation of 11.1, 17.7, and 11.3%, respectively, for three healthy subjects over three MRSI scans.

In Vivo ^{31}P MRSI: HCC Patient

Figure 8 shows the ^{31}P MRSI dataset obtained from a HCC patient (M, 78 years). The malignant tumor of about 2.5 cm diameter can clearly be observed in the ^{1}H image obtained with our coil in the top right panel. The gradient recalled echo images displayed in the figure were acquired thirty minutes post Gadolinium contrast administration. An enlarged liver in the ^{1}H scan of this patient is observed due to the presence of ascites. The bottom part of the figure shows ^{31}P spectra obtained from a voxel mainly covering malignant tissue (left) and a voxel from nonmalignant liver tissue (right). An increase of the PME peak and a decrease of the PDE peak are seen in the malignant liver tissue compared to the nonmalignant tissue, which agrees with the results presented in (30). Analysis of the PME/PDE ratio for the patient gave a
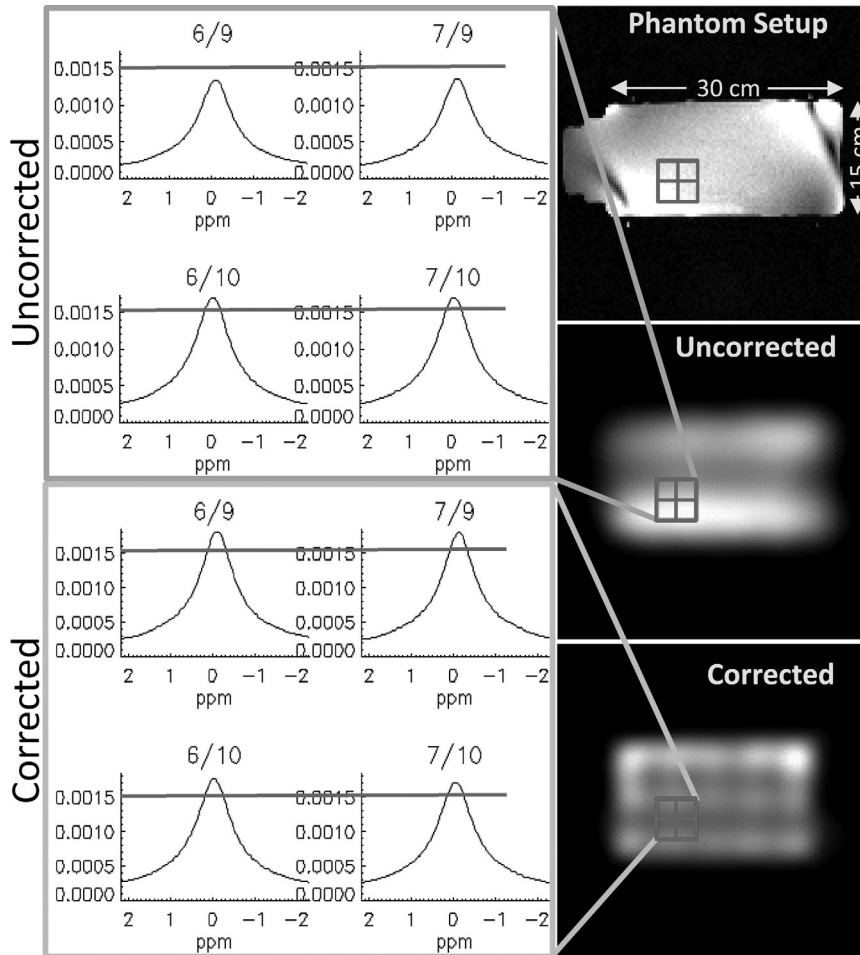
FIG. 6. Uncorrected and corrected MRSI data from a phantom containing a uniform Pi solution. The ¹H image of the phantom setup appears on the right with uncorrected and corrected Pi metabolite maps obtained by plotting the area under the Pi peak before and after sensitivity correction. The square ROI displayed on the images consists of four voxels with Pi peak variance across the 2 × 2 array of voxels. The Pi peaks corresponding to the voxels in the ROI are shown on the left side of the figure. The horizontal line on each of the Pi spectra is merely a reference to better illustrate the variation in peak height due to coil sensitivity.

value of 0.76 in the tumor voxel (dashed line) and 0.52 in the nonmalignant voxel (solid line), resulting in a difference of 37%. This result demonstrates that the variability observed in the data for intrasubject scans (average of 23.3% as shown in the previous section) is smaller than the difference observed between malignant and nonmalignant tissue. Furthermore, reproducibility analysis performed on two pretreatment ^{31}P MRSI scans of another HCC patient (F, 57 years) gave a scan-to-scan variability of 17.1% in the PME/PDE ratio from the voxel-containing tumor. This additional finding indicates that the variability in pretreatment ^{31}P tumor metabolite measurements can be within the normal intrasubject variability range.

DISCUSSION

These results show that our multichannel dual-tuned phased-array ^{31}P/^{1}H coil can obtain ^{31}P and ^{1}H data across an entire axial slice of the abdomen. This extended coverage is necessary for several applications requiring sensitivity throughout the whole liver (e.g., examining lesions in the middle of the body or multiple lesions). The coil can also be used for conventional ^{1}H MR imaging of the entire abdomen during the same scan session without repositioning the patient to exchange coils, thereby minimizing reproducibility errors and the

patient's examination time. Even though the images acquired with our coil have a slightly lower SNR than a dedicated ^{1}H torso coil array, the image quality is sufficiently high for most clinical needs, and is superior to the quality of body coil images. Compared to images acquired with a single surface coil only, they have the advantage of a much larger anatomic coverage.

Most of the liver ^{31}P spectroscopy results published so far have used single channel ^{31}P surface coils. Typical diameters of these coils vary from a minimum of 9 cm (8) to a maximum of 16 cm (11). The only exception was the heart/liver coil used by Tosner et al. (20), with a 12 × 27.5 cm² ^{31}P TX coil and 14 × 12 cm² (single-turn) + 9 × 9 cm² (figure-eight loop) ^{31}P RX elements. In comparison, our TX and RX coils for ^{31}P are much larger with four ^{31}P RX elements, each about 24 × 20 cm², and one ∼ 30 × 30 cm² ^{31}P TX element on both anterior and posterior plates—a combination that provides larger coverage. Typically, at a depth of one diameter, the sensitivity of a surface coil is reduced to 10% of its maximum value (31). Analysis of our coil shows that it is sensitive through a depth of 20 cm (although each individual plate is only sensitive to a maximum depth of 10 cm). Note that this current maximum sensitivity depth of 20 cm is obtained using a purely empirical cut off value of 25% of the maximum signal. (Below this cutoff, the signal from the coil could not be quantified.) The 25% cutoff
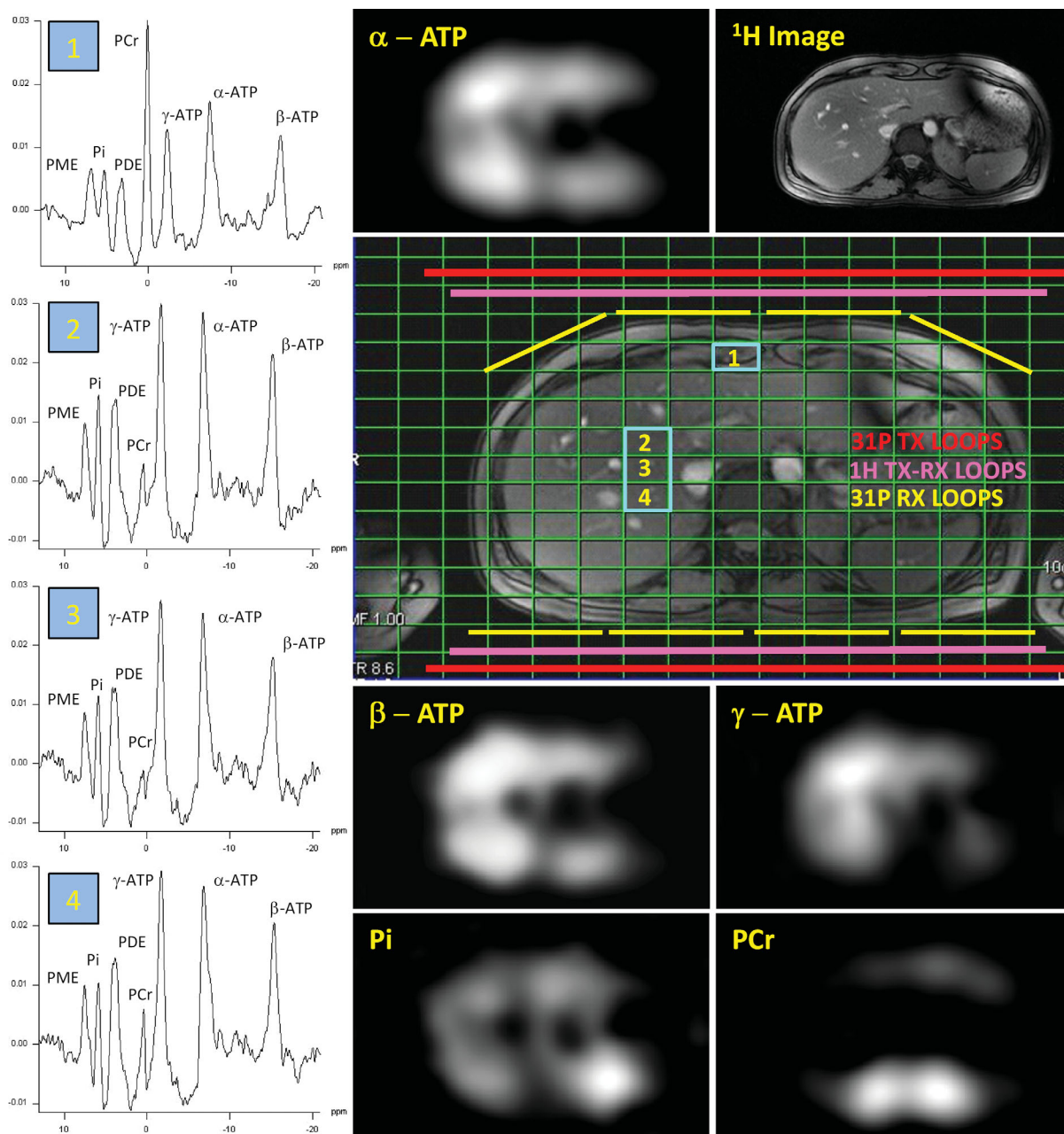
FIG. 7. Position of various coil loops with respect to the abdomen, sample spectra from four voxels (one close to the surface containing abdominal muscle and three from liver tissue), and phosphorus metabolite maps of the 2D MRSI slice. In this subject, the new coil provided full anatomic coverage for ^{31}P MRSI throughout the axial slice. The ^{1}H image in the top right corner is scaled to match the ^{31}P metabolite maps.

Table 1

Variability Results for PME/PDE Ratios Obtained From Three Healthy Volunteers for Three Different Scans

Average over 10 voxels	PME/PDE			% Difference PME/PDE			Average % difference
	Scan 1	Scan 2	Scan 3	Scan 1–2	Scan 1–3	Scan 2–3	
Subject 1 (F, 39 years)	0.37	0.31	0.33	27.6	20.0	20.9	22.8
Subject 2 (F, 34 years)	0.40	0.41	0.39	19.6	23.2	22.3	21.7
Subject 3 (M, 26 years)	0.72	0.65	0.67	21.4	27.8	17.9	22.4

PME/PDE ratios were averaged over 10 voxels, as illustrated in Fig. 5 and described by Eq. 3. Note that the intrasubject variation in the average value of the PME/PDE ratio is clearly less than the intersubject variation.

Table 2
Mean Values of PDE/β-ATP, Pi/β-ATP, and PME/β-ATP Ratios Over Three Scans, and Average Percent Variation of the Ratios Between Scans 1–2, 1–3, and 2–3

Averaged over 10 voxels and three scans	PDE/β -ATP		Pi/β -ATP		PME/β -ATP	
	Average	% Difference	Average	% Difference	Average	% Difference
Subject 1 (F, 39 years)	1.04	1.2	0.44	11.6	0.33	7.2
Subject 2 (F, 34 years)	0.92	10.8	0.39	15.6	0.41	10.9
Subject 3 (M, 26 years)	0.73	21.3	0.54	25.8	0.41	15.9

corresponds specifically to the current coil design and acquisition protocol and will potentially change with further improvements.

The scan times reported in previous ^{31}P MRS liver studies varied from 4 min (32) to 34 min (10,13). However, average scan times reported in most of the studies were about 20 min, which is comparable to the 24 min scan time of our protocol. The average voxel size from which ^{31}P liver data was collected varied from a minimum of $1.5 \times 1.5 \times 1.5$ cm[3] (21) to as large as $40 \times 10 \times 4$ cm[3] (11) in single voxel studies. However, the nominal voxel sizes used for ^{31}P MRSI studies were mostly around $4 \times 4 \times 4$ cm[3]. With a nominal voxel size of $2.5 \times 2.5 \times 2.5$ cm[3], our coil offers higher resolution as well as full slice coverage. To test the current protocol limita-

tions, an even higher resolution 45 min in vivo scan was acquired with a scan matrix of $26 \times 16 \times 1$ and nominal voxel size of $1.56 \times 1.54 \times 2.5$ cm[3]; however, this scan could not provide adequate SNR throughout the entire abdominal axial slice. Further optimization of the coil design and the protocol is required before the coil can be used for a higher resolution clinical study.

For an initial pilot study on patients, the selection criterion of a malignant focal hepatic lesion of at least 1 cm in diameter was used, given the spatial resolution of our protocol. Furthermore, considering the depth limitation of the coil's sensitivity, it is estimated that only 30–40% of all patients with focal liver lesions would benefit from the full sensitivity of the coil throughout the abdomen. However, if we focus on subjects with focal liver lesions within
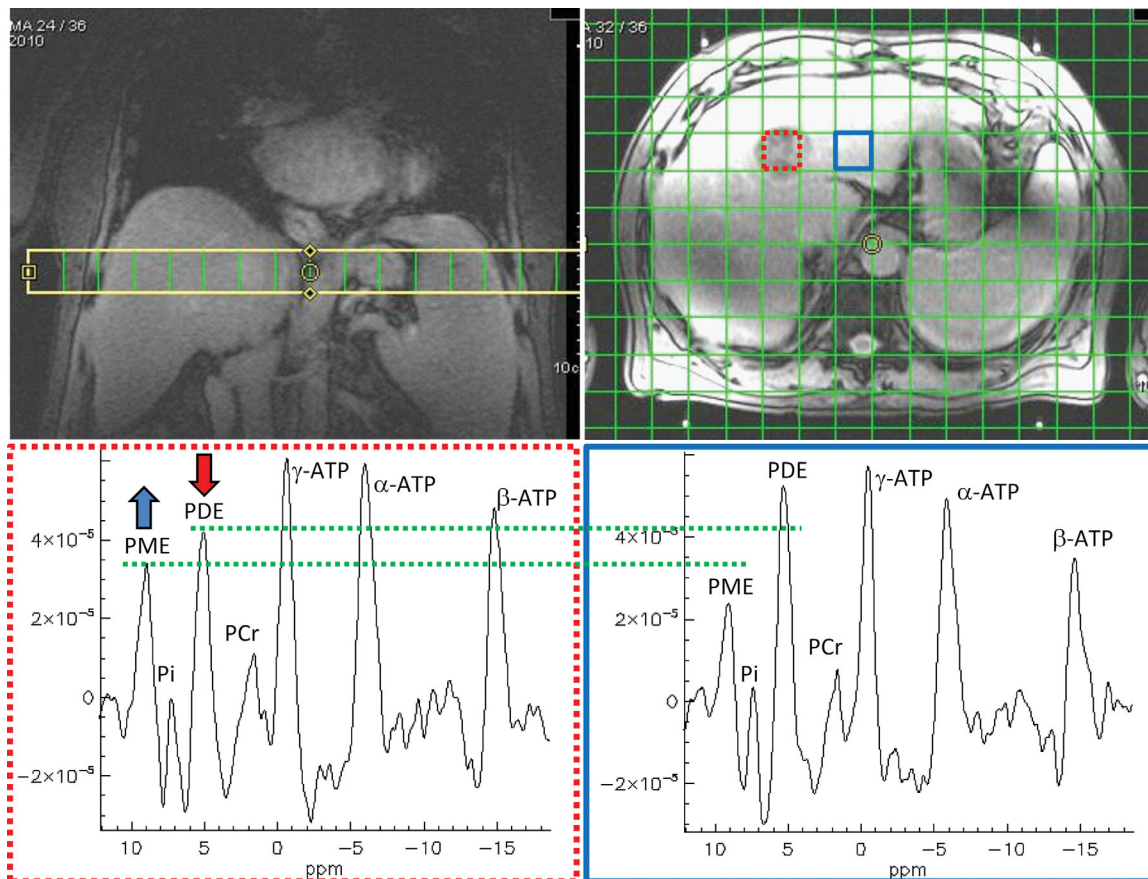

FIG. 8. [31]P spectroscopic data obtained from a liver cancer patient. The ^{1}H images on the top left and right show the MRSI grid placement on the coronal and transverse views, respectively. The spectrum on the left is from malignant liver tissue, showing increased PME and decreased PDE compared to the spectrum on the right from nonmalignant liver tissue in the same patient. [Color figure can be viewed in the online issue, which is available at wileyonlinelibrary.com.]

10 cm from the surface, we expect a successful ^{31}P MRSI exam from 65 to 75% patients treated at our clinical site.

A 10-mmol/L phosphorus concentration phantom was chosen for coil characterization because the in vivo liver concentration of PDE is about 10 mmol/L (21). As we are primarily interested in investigating PME and PDE peaks, using this concentration gives us realistic sensitivity maps and coil characteristics for in vivo data acquisition. We note that the ^{31}P concentration of our phantom is much smaller than the 20–75 mmol/L used in previous ^{31}P studies (9,21). Our coil was designed with a calibrated TX signal to be equally sensitive for the top and bottom ^{31}P TX coils (−35.4 and −35.7 dB, respectively). However, our phantom experiments show the top coil to be slightly less sensitive compared to the bottom coil. A possible reason might be the loading difference between the coils because of the curvature of the top coil plate.

The average PME/PDE values calculated over 10 voxels for subjects 1 and 2 are within the reported range of 0.18–0.50 from previous studies (8,21,33); however, for subject 3, the average PME/PDE value of 0.68 is larger, which may be explained by the much smaller PDE values observed in this subject compared to the other subjects. As shown in Fig. 5, we quantified an average of at least 10 voxels per subject for the variability analysis. An intrasubject variability of 16–27% was reported by (3,10,20). Sijens et al. (32) reported a 10–13% variation in metabolite peak areas derived from liver MRSI measurements with 15–17% variation for PME and PDE. Compared to these values, our intrasubject variability of 19.6–27.8% is within the reported range for free breathing acquisitions. Much smaller variability in PME (1.82%) and PDE (2.93%) was reported by Chmelik et al. (21), when the movement due to breathing was constrained by acquiring the data with subjects lying in the prone position.

An increase in PME and a decrease in PDE, resulting in an elevated PME/PDE ratio in liver cancer compared to healthy liver tissue, have been consistently reported in many ^{31}P studies (3,30,34). Our data collected from an HCC subject yielded a PME/PDE value of 0.76, which is close to the lower end of the PME/PDE range (0.83–1.47) reported by (3) for HCC patients; however, our value is higher than the value of 0.71 found by Glazer et al. (34) averaged over several malignant tumors (most of which were HCC tumors). In our study, the PME/PDE value found in a nonmalignant liver tissue voxel in the same patient was 0.52, which is again consistent with the reported values for healthy liver tissue. Analysis of the ^{31}P MRSI data for the healthy subjects and the patient with HCC clearly showed that the variability observed in the data from one scan session to another for the same subject is smaller than the difference observed between malignant and nonmalignant tissue. Therefore, our coil has the potential to be sensitive enough to detect changes in tumor metabolism, such as changes in PME and PDE peaks in malignant tissue that correlate with treatment success.

A scan time of 24 min for a single MRSI scan is still rather long to be included in clinical MRI protocols and is prone to motion artifacts. Therefore, a next step will be to reduce the scan time by using GRAPPA (35), which we have demonstrated successfully with our coil on phantoms (36). To regain the necessary SNR, expand coverage, and enable the use of nonslice-selective adiabatic excitation pulses, a 3D ^{31}P MRSI sequence is currently being optimized. Using GRAPPA might also allow us to use respiratory-gated 2D or 3D ^{31}P MRSI while keeping the overall scan time on the order of 20 min, which should further reduce the variability of the data. The SNR performance and uniformity of the coil could also be improved by incorporation of B1-insensitive excitation pulses like adiabatic half passage (AHP) pulses in the current protocol. More homogeneous excitation should further improve clinical performance.

In conclusion, our novel ^{31}P/^{1}H dual-tuned multichannel coil enables the measurement of ^{31}P metabolites from liver lesions located in deep tissue, while also providing clinically useful proton images with good SNR during the same scan session. Various techniques (water filled fiduciary markers, permanent markers on the scanner bed and coil surface) have proven successful in minimizing data variability associated with coil placement and spectroscopic planning. We, therefore, expect that this optimized setup for ^{31}P MRSI data collection with a coil sensitive to the whole liver may be successfully used to monitor the response to targeted radiation treatment in liver lesions. However, further improvements such as reduced scan time or reduced sensitivity to motion are still needed to better integrate ^{31}P spectroscopy into the clinic.

REFERENCES

1. Solga SF, Horska A, Clark JM, Diehl AM. Hepatic 31P magnetic resonance spectroscopy: a hepatologist's user guide. Liver Int 2005;25: 490–500.
2. Dagnelie PC, Leij-Halfwerk S. Magnetic resonance spectroscopy to study hepatic metabolism in diffuse liver diseases, diabetes and cancer. World J Gastroenterol 2010;16:1577–1586.
3. Cox IJ, Bell JD, Peden CJ, Iles RA, Foster CS, Watanapa P, Williamson RC. In vivo and in vitro 31P magnetic resonance spectroscopy of focal hepatic malignancies. NMR Biomed 1992;5:114–120.
4. Vente MA, Wondergem M, van der Tweel I, van den Bosch MA, Zonnenberg BA, Lam MG, van Het Schip AD, Nijsen JF. Yttrium-90 microsphere radioembolization for the treatment of liver malignancies: a structured meta-analysis. Eur Radiol 2009;19:951–959.
5. Schefter TE, Kavanagh BD, Timmerman RD, Cardenes HR, Baron A, Gaspar LE. A phase I trial of stereotactic body radiation therapy (SBRT) for liver metastases. Int J Radiat Oncol Biol Phys 2005;62: 1371–1378.
6. Ford JM, Sandrasegaran K, McLennan G, Wertman DE Jr, Agarwal DM. Yttrium-90 (Y-90) Intra-arterial brachytherapy therapy for hepatocellular carcinoma. In: Proceedings of the 93rd Annual Meeting of RSNA, Chicago, Illinois; 2007. p 776.
7. Price TR, Perkins SM, Sandrasegaran K, Henderson MA, Maluccio MA, Zook JE, Tector AJ, Vianna RM, Johnstone PAS, Cardenes HR. Evaluation of response after stereotactic body radiation therapy for hepatocellular carcinoma. Int J Radiat Oncol Biol Phys 2009;75: S677–S678.

8. Meyerhoff DJ, Karczmar GS, Matson GB, Boska MD, Weiner MW. Non-invasive quantitation of human liver metabolites using image-guided 31P magnetic resonance spectroscopy. NMR Biomed 1990;3: 17–22.

9. Buchli R, Duc CO, Martin E, Boesiger P. Assessment of absolute metabolite concentrations in human tissue by 31P MRS in vivo. Part I: cerebrum, cerebellum, cerebral gray and white matter. Magn Reson Med 1994;32:447–452.

10. Li CW, Negendank WG, Murphy-Boesch J, Padavic-Shaller K, Brown TR. Molar quantitation of hepatic metabolites in vivo in proton-decoupled, nuclear Overhauser effect enhanced 31P NMR spectra localized by three-dimensional chemical shift imaging. NMR Biomed 1996;9:141–155.

11. Sijens PE, Van Dijk P, Dagnelie PC, Oudkerk M. Non-T1-weighted 31P chemical shift imaging of the human liver. Magn Reson Imaging 1995;13:621–628.

12. Murphy-Boesch J, Jiang H, Stoyanova R, Brown TR. Quantification of phosphorus metabolites from chemical shift imaging spectra with corrections for point spread effects and B1 inhomogeneity. Magn Reson Med 1998;39:429–438.

13. Zakian KL, Koutcher JA, Malhotra S, Thaler H, Jarnagin W, Schwartz L, Fong Y. Liver regeneration in humans is characterized by significant changes in cellular phosphorus metabolism: assessment using proton-decoupled 31P-magnetic resonance spectroscopic imaging. Magn Reson Med 2005;54:264–271.

14. Schmid AI, Chmelik M, Szendroedi J, Krssak M, Brehm A, Moser E, Roden M. Quantitative ATP synthesis in human liver measured by localized 31P spectroscopy using the magnetization transfer experiment. NMR Biomed 2008;21:437–443.

15. Matson GB, Vermathen P, Hill TC. A practical double-tuned 1H/31P quadrature birdcage headcoil optimized for 31P operation. Magn Reson Med 1999;42:173–182.

16. Greenman RL, Rakow-Penner R. Evaluation of the RF field uniformity of a double-tuned 31P/1H birdcage RF coil for spin-echo MRI/MRS of the diabetic foot. J Magn Reson Imaging 2005;22:427–432.

17. Duan Y, Peterson BS, Liu F, Brown TR, Ibrahim TS, Kangarlu A. Computational and experimental optimization of a double-tuned (1)H/(31)P four-ring birdcage head coil for MRS at 3T. J Magn Reson Imaging 2009;29:13–22.

18. Hardy CJ, Bottomley PA, Rohling KW, Roemer PB. An NMR phased array for human cardiac 31P spectroscopy. Magn Reson Med 1992; 28:54–64.

19. Nakada T, Kwee IL, Miyazaki T, Iriguchi N, Maki T. 31P NMR spectroscopy of the stomach by zig-zag coil. Magn Reson Med 1987;5: 449–455.

20. Tosner Z, Dezortova M, Tintera J, Hajek M. Application of two-dimensional CSI for absolute quantification of phosphorus metabolites in the human liver. MAGMA 2001;13:40–46.

21. Chmelik M, Schmid AI, Gruber S, Szendroedi J, Krssak M, Trattnig S, Moser E, Roden M. Three-dimensional high-resolution magnetic resonance spectroscopic imaging for absolute quantification of 31P metabolites in human liver. Magn Reson Med 2008;60:796–802.

22. Wright SM, Wald LL. Theory and application of array coils in MR spectroscopy. NMR Biomed 1997;10:394–410.

23. American College of Radiology (ACR). Phantom test guidance for the ACR MRI Accreditation Program. Reston, VA; 1998.

24. Pohmann R, von Kienlin M. Accurate phosphorus metabolite images of the human heart by 3D acquisition-weighted CSI. Magn Reson Med 2001;45:817–826.

25. NEMA Standards Publication MS 8–2008. Characterization of the specific absorption rate for magnetic resonance imaging systems.

26. James J, Lin C, Dydak U, Babsky A, Stark H, Dale B, Bansal N. Sodium MR Imaging at 3T Using an 8-Channel 23Na and 2-Channel 1H Rx/Tx Coil: optimization and RF inhomogeneity corrections. In: Proceedings of the 17th Annual Meeting of ISMRHonolulu M, Hawaii, USA; 2009. p 614.

27. Vanhamme L, van den Boogaart A, Van Huffel S. Improved method for accurate and efficient quantification of MRS data with use of prior knowledge. J Magn Reson 1997;129:35–43.

28. Naressi A, Couturier C, Devos JM, Janssen M, Mangeat C, de Beer R, Graveron-Demilly D. Java-based graphical user interface for the MRUI quantitation package. MAGMA 2001;12:141–152.

29. Hamilton G, Patel N, Forton DM, Hajnal JV, Taylor-Robinson SD. Prior knowledge for time domain quantification of in vivo brain or liver 31P MR spectra. NMR Biomed 2003;16:168–176.

30. Dagnelie PC, Sijens PE, Kraus DJ, Planting AS, van Dijk P. Abnormal liver metabolism in cancer patients detected by (31)P MR spectroscopy. NMR Biomed 1999;12:535–544.

31. de Graaf RA. In vivo NMR spectroscopy: principles and techniques, 2nd ed. Wiley: Chichester; 2008. p 524.

32. Sijens PE, Dagnelie PC, Halfwerk S, van Dijk P, Wicklow K, Oudkerk M. Understanding the discrepancies between 31P MR spectroscopy assessed liver metabolite concentrations from different institutions. Magn Reson Imaging 1998;16:205–211.

33. Buchli R, Meier D, Martin E, Boesiger P. Assessment of absolute metabolite concentrations in human tissue by 31P MRS in vivo. Part II: Muscle, liver, kidney. Magn Reson Med 1994;32:453–458.

34. Glazer GM, Smith SR, Chenevert TL, Martin PA, Stevens AN, Edwards RH. Image localized 31P magnetic resonance spectroscopy of the human liver. NMR Biomed 1989;1:184–189.

35. Griswold MA, Jakob PM, Heidemann RM, Nittka M, Jellus V, Wang J, Kiefer B, Haase A. Generalized autocalibrating partially parallel acquisitions (GRAPPA). Magn Reson Med 2002;47:1202–1210.

36. Raghavan RS, Panda A, Valette J, James J, Heberlein K, Boettcher U, Henry P, Bansal N, Dydak U. 31P Spectroscopic Imaging with GRAPPA. In: Proceedings of the 17th Annual Meeting of ISMRHonolulu M, Hawaii; 2009. p 4317.